Materials & Design 241 (2024) 112920

Contents lists available at ScienceDirect

Materials & Design

journal homepage: www.elsevier.com/locate/matdes

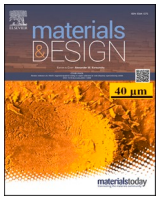

Unlocking the Dual Helical Ribbon for rotational viscosity measurements of highly heterogeneous fluids

G. Giancontieri [a], D.M. Hargreaves [b], P. Partal [c], D. Lo Presti [a,*]

[a] Dipartimento di Ingegneria, Universita degli studi di Palermo, Italy
[b] Faculty of Engineering, University of Nottingham, Nottingham NG7 2RD, UK
[c] Pro²TecS-Chemical Process and Product Technology Research Centre, Department of Chemical Engineering, ETSI. Campus de "El Carmen", Universidad de Huelva, 21071 Huelva, Spain

ARTICLE INFO

Keywords:
Rheometry
Rheology
Dual Helical Ribbon
Computational Fluids Dynamic
Heterogeneous Fluids
Viscosity

ABSTRACT

Road bituminous binders are becoming more complex since, to enhance properties and/or engineer circular economy, the conventional binder is enriched with modifiers of different nature giving birth to a final-product recognisable as highly heterogeneous fluid. The assessment of these materials relies on rheological measurements; however, existing testing equipment are designed for homogeneous fluids, proving to be often inadequate. In fact, rotational testing lacking mixing efficiency during measurements, can compromise sample stability, resulting in non-representative results Lo Presti et al. (2014). To address these challenges, a dual helical ribbons (DHR) was purposefully created and successfully employed in prior studies to measure the rotational viscosity of highly heterogeneous asphalt materials Giancontieri et al. (2019). While the DHR effectiveness has been extensively discussed in earlier investigations, this study aims to contribute to the scientific community at large by providing: state-of-the-art on improving mixing efficiency of highly heterogeneous fluids, rationalizing the choice of the DHR geometry comprehensive technical details for realising any DHR, verified through numerical modelling Calibration with model input parameters achieved by adopting the Rieger and Novak method, and finally design validation. The authors aim for the broader material science community to benefit from this investigation, enabling technologists to independently develop DHR devices and explore new applications.

1. Introduction

In modern industrial processes, it is common to deal with heterogeneous fluids that deviate from Newtonian behavior, meaning they exhibit non-uniform characteristics. Industrial applications encompass a diverse array of fields where heterogeneous fluids play a prominent role. These fluids are encountered in numerous scenarios, such as in multiphase mixtures like emulsions, suspensions, foams, and dispersions [3]. They are also found in high molecular weight systems and their solutions, including polymers, proteins, and gums [4]. Moreover, heterogeneous fluids are integral to the production of various products, including foods, pharmaceuticals, personal care items, agricultural chemicals, lubricants, and slurry fuels.[1,4–7]. The experimental characterisation of a material's rheological properties is of utmost significance not only in the design phase but also throughout its development, performance, and application. Nevertheless, when it comes to heterogeneous materials, achieving accurate and realistic rheological measurements continues to be a challenging task.

For example, Fig. 1.1 shows the behaviour of a particulate suspension using different geometries such as a dual helical impeller, a cylindrical and a vane spindle during rotational testing. The figure clearly shows the settling and migration of the particulates away from the cylindrical gap. Thus, phase separation, sedimentation, agglomeration etc. can take place in the sample while is tested in the measuring chamber. These phenomena affect the sample stability and can lead to results that are not reproducible and unrepresentative of the original sample. In a laboratory, usually rotational viscometers with a cup and bob setup are used for this purpose. The configuration involves a tube where the sample is poured, along with a selected geometry that is inserted and subsequently rotated at a predetermined speed. By measuring the applied torque, the viscometer can provide a viscosity reading for the test fluid.

The above set-up was designed for homogeneous systems but continues to be used for a wide range of materials, no matter the complexity.

* Corresponding author.
E-mail address: davide.lopresti@unipa.it (D. Lo Presti).

https://doi.org/10.1016/j.matdes.2024.112920
Received 22 October 2023; Received in revised form 2 April 2024; Accepted 6 April 2024
Available online 8 April 2024

These types of issues are commonly encountered when measuring the viscosity of various materials such as, plastic, food, cosmetics, paints, asphalt binders and, lubricants [2,4,5,7–13]. To address those issues, rotational viscometers are commonly supplied with a set of different geometries specifically conceived to aid rheologists in accurately assessing the viscosity of such materials. These accessories are useful for specific applications but may not be able to ensure the sample stability during rotational tests for heterogeneous systems that tend to stratify due to differences in phase density, as can be seen in Fig. 1.1. In an effort to improve the accuracy of rheological measurements on highly modified asphalt binders, [14] authors designed an helical impeller (DHI) for rotational viscometers. They conducted experiments to determine if the DHI could enhance the homogenization of high viscosity fluids, thereby reporting more consistent viscosity readings. When compared to the standard coaxial geometry used by Brookfield, the DHI consistently reported a different "apparent" viscosity. "Apparent viscosity" refers to the viscosity that is calculated using a non-conventional geometry, such as the DHI. In the case of a cylindrical geometry, the viscosity can be related to a simple theory because the flow between the cylinders can be described mathematically. However, with a complex impeller like the DHI, a series of tests using standard fluids of known viscosity must be conducted to create a library of torque versus viscosity curves. In summary, the use of non-conventional geometry, such as the DHI, does not directly measure the absolute viscosity. The researchers found that the DHI produced more consistent results due to its ability to create axial pumping within the sample, compared to the tangential flow generated by the conventional coaxial geometry (SC-27). However, while the experimental campaign yielded positive results, the mechanism behind the enhanced mixing achieved by the helical geometry and the magnitude of this improvement have not been comprehensively clarified. In a follow-up study, Lo Presti [15], combined experimental and computational methods to gain further insight into the DHI's performance. The authors found that the DHI represented a significant advancement in testing geometries for viscosity measurements of heterogeneous fluids, particularly in product development. However, both numerical and experimental results indicated that the DHI allowed for a good mixing of volume fractions. However, due to the narrow gap between the inner central screw and outer helix, it experienced clogging issues, particularly when using crumb rubber particles or suspensions prone to agglomeration. This led to misleading results being reported. Therefore, when working with heterogeneous materials, there was still a need to improve the impeller design and the interpretation of the results to further enhance the accuracy of viscosity measurements. In a further study Giancontieri [16] successfully introduced a dual helical ribbon (DHR) impeller particularly designed to address the above mentioned technical issue occurring during rotational viscosity measurements of highly heterogeneous fluids.

Several research further demonstrates laboratory applications where the DHR proves advantageous: improving stability during rotational viscosity measurements of heterogeneous materials and allowing using rotational viscometer as a low shear mixer with real-time monitoring capabilities (Table 1). In the first application, [2] developed for high temperature rotational viscosity measurements on highly heterogeneous binders, the impeller was used with a Brookfield viscometer in place of a conventional cylindrical spindle and viscosity measurements were carried out on recycled tyre rubber modified binders (RTR-MB) and

Table 1
Summary of DHR Applications as an impeller for rheological measurements of bituminous materials.

	Applications	Viscosity Range (PaS)	Materials	DHR	Reference
1	Product development with real-time monitoring of rheological properties (190°C)	0.2–1	• Crumb rubber modified binders. Polymer modified bitumen	DHR 1.0 DHR 2.0	[11,17]
2	Quality control with real-time monitoring of rheological properties during hot storage (190-150°C)	0.2–3	• Crumb rubber modified binders. Polymer modified bitumen	DHR 2.0	[17]
3	Rotational viscosity measurements of bituminous binders (100-180°C)	0.5–2.5	• Neat Bitumen Crumb rubber modified binders. Polymer modified bitumen. Polyethylene modified bituminous binders	DHR 2.0	[2,10,12]
4	Rotational viscosity measurements of bituminous emulsions (10-40°C)	0.01–1	• Cold bitumen emulsion slurries	DHR 1.0	[18]

Fig. 1.1. Rheological measurement problems with practical oil-particles emulsions using different testing geometry, a dual helical impeller on the left, a cylindrical spindle in the centre (SC-27) and a vane spindle on the right. Initially, the sample contained in the tubes may be homogeneous. After some time, the sample may become quite stratified.

polymer modified binders (PMB). Results showed that the DHR provided more realistic trend of measurements thanks to its ability to guarantee the sample stability while performing rotational testing. In a further study, Mignini [18] took advantage of the enhanced mixing performance provided by the DHR to successfully characterise the rheological properties of a wide range of cold bitumen emulsion slurries. In a further application [2] the adoption of the DHR was advised for the real-time monitoring of crumb rubber modified (CRM) binders during production and hot storage (Fig. 1.2). Several investigations have demonstrated the potential of employing rotational viscometers to simulate the production of CRM binders, however due to the lack of mixing provided by standard geometries this procedure was not fully exploited. The DHR, instead provided promising results and the research extended the possibility of governing the binders' modification process also to the hot storage phase.

1.1. Aim and structure of the paper

This study's objective is to share technical knowledge with material scientists, specifically focusing on the design, calibration, and validation of the DHR. By disseminating these details, it provides the essential information required for the potential implementation of this technology in yet-to-be-discovered applications. The study is divided into different steps/tasks related together as shown in Fig. 1.3 by introducing an innovative combined experimental–numerical approach aimed to identify, calibrate, and manufacture an optimal geometry for rotational viscosity testing of highly heterogeneous fluids. A state-of-the-art on mixing geometries able to guarantee the sample stability was carried out and a new geometry identified, the dual helical ribbon (DHR) impeller. The new geometry was designed and verified by means of numerical modelling. Multiphases simulations of know viscosity fluids with suspended particles were run by comparing the DHR and a coaxial cylinder configuration (SC-27) to provide useful information about potential technical issues happening during rotational testing. The computational platform provided a further support to evaluate and monitor the sample stability of these materials that otherwise would have been difficult if not impossible to visualise during conventional laboratory test. Following the encouraging numerical results, first, to avoid expensive and time-consuming manufacturing procedures, a prototype was realised by using the 3D printing technology showing outstanding results. Finally, the DHR was manufactured in stainless steel, it was calibrated by using the Rieger and Novak method and then validated by performing measurements of a highly heterogeneous fluid of known viscosity. The investigation also shows two novel applications of the DHR for asphalt binders, both relying on improved sample stability and, in turns, more realistic viscosity measurements. At last, the discussion and conclusion section provides the main take away messages for those eager to tailor the proposed approach to their own field of study.

2. Mixing efficiency optimisation

2.1. Measuring viscosity by means of a rotational viscometer

For rotational viscometry using coaxial cylinders, there is a theoretical basis to calculate viscosity. It involves a rotating cylinder, with radius R_s and length, L, inside a stationary cylinder of radius, R_c at an angular velocity, ω,[3]. The shear rate,$\dot{\gamma}$, at the spindle surface can be calculated as follows:

$$\dot{\gamma} = \frac{2\omega R_c^2}{R_c^2 - R_s^2} \tag{1}$$

and the shear stress, τ, is.

$$\tau = \frac{T}{2\tau R_s^2 L} \tag{2}$$

where T is the torque input by the machine. The viscosity,μ is

$$\mu = \frac{\tau}{\dot{\gamma}} = \frac{T\left(R_C^2 - R_S^2\right)}{4\pi\omega R_C^2 R_s^2 L} \tag{3}$$

Equation 3 simplifies viscosity determination as all variables are measurable. However, when a non-cylindrical geometry is used, equations for shear rate and shear stress, similar to Equation 2 and Equation 3 are not available. This poses a challenge, as the impellers may be effective for mixing but do not provide a straightforward method to determine mixture viscosity. By directly measuring the torque (T) and angular velocity (ω), the viscosity can be determined.

To do that, the impeller design has to be calibrated using a wide range of silicone viscosity standard fluids with known viscosity, commonly used to verify calibration of viscometers. This allows for the determination of viscosity as a function of torque and angular velocity.

$$\mu = \mu(T, \omega) \tag{4}$$

The calibration procedure becomes more complex as it would need to be conducted separately for each class of fluid. Additionally, the operator would need to determine and classify the fluid into the appropriate class. This adds an additional layer of decision-making and complexity to the calibration process. An alternative procedure is introduced by Brookfield and demonstrated in [8]. When using a Brookfield viscometer

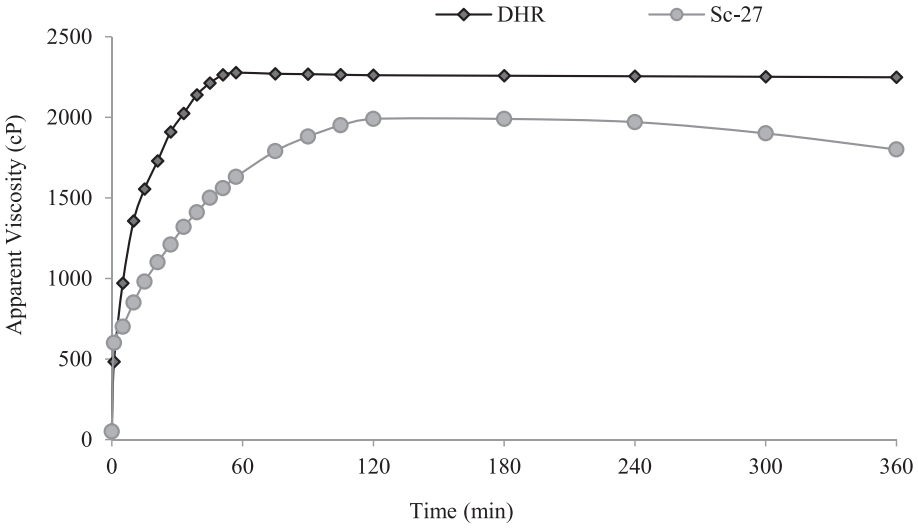

Fig. 1.2. Real-time monitoring of the binder's production stage (177.5 °C, 50 Rpm) of a 18 % CRM [2].

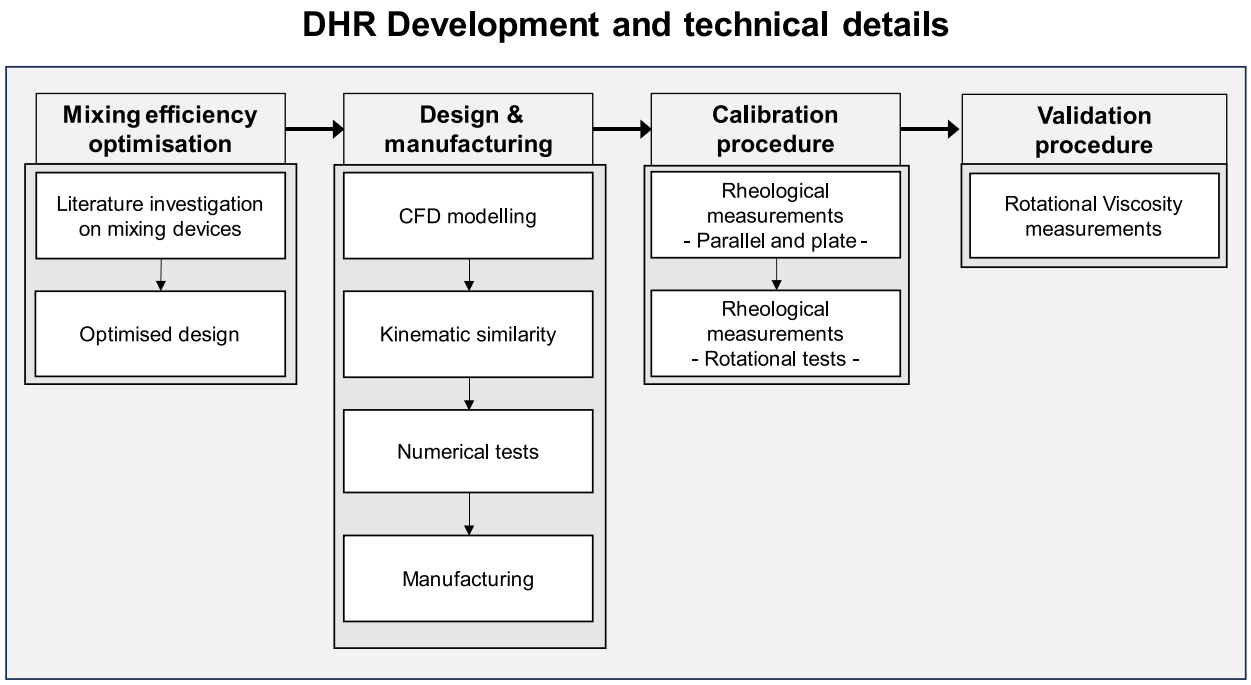

Fig. 1.3. Summary of the methodology used in this work and results provided to the scientific community working in material science.

each spindle geometry is correlated to a Spindle Multiplier Constant (SMC), which facilitates the determination of apparent viscosity from the following equation:

$$\mu = \frac{0.1}{N} \cdot TK \cdot SMC \cdot T\% \tag{5}$$

Where TK is torque constant, N is the rotational speed (Rpm) and $T\%$ is maximum value of torque, in percentage, allowable by the machine. Finally, the apparent shear rate $\dot{\gamma}$, where SRC is the Shear Rate Constant, is defined as

$$\dot{\gamma} = SRC\hat{A} \cdot N = SRC\hat{A} \cdot \left(\frac{60}{2\pi}\right)\omega \tag{6}$$

Lo Presti [1] tried to calibrate the DHI by matching an SMC value offered by Brookfield for the cylindrical spindles, the SC-XX ranges, which have specific values. Nevertheless, the common viscometer only permits the user to select a code, preventing fine adjustments. The authors were able to match the DHI with a spindle code by testing it against known viscosity fluids. This approach was useful for obtaining values of apparent viscosity while using the DHI, however its validity is open to questions.

2.2. Experimental studies

A literature study was carried out aimed to identify which type of impeller geometry can guarantee the sample stability while performing rotational measurements. The blending of high viscosity multiphase fluids, including solid/liquid or liquid/gas mixtures, is a common challenge in the production of asphalt blends, coatings, minerals, food, pharmaceuticals, polymers, metallurgical products, biochemicals, and other industrial processes. [19–21]. Researchers have proposed various types of impellers to address this challenge (as seen in Fig. 2.1). These designs include those with large impeller diameter or those with close-clearance, such as anchors and helical ribbons, as reported in studies [22–26].

Traditionally, this procedure is conducted within agitated containers, and it has been extensively proven that helical ribbon impellers are the most effective choice for mixing both high-viscosity Newtonian

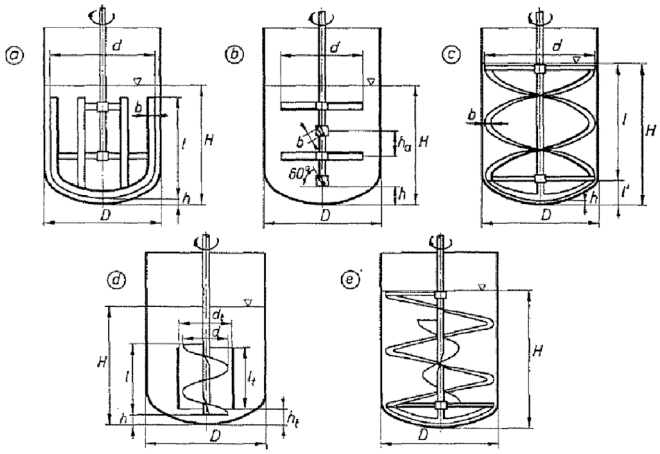

Fig. 2.1. The drawings of the most investigated impellers. a) anchor impeller, b) multi-paddle, c) helical ribbon, d) and e) helical ribbon screw impellers. [22].

[27] and non-Newtonian fluids [28]. Prior to the advent of numerical simulations, the selection of mixers was typically conducted through experimental means, employing various measures including power consumption [29–32], mixing time [33,34] and circulation time [23].

Helical ribbon performances are more suitable to mix highly viscous liquids thanks to two fundamental mechanisms:

- The shear deformation induced by the impeller in the fluid, specifically in the gap between the blade and the vessel wall, leads to increased homogeneity of the mixture with higher levels of deformation.
- The pumping action of the impeller creates axial flow, facilitating the renewal of the fluid in the gap.

The primary flow allows to reduce the overall level of heterogeneity as the deformation is increased. In contrast, the axial pumping facilitates the recirculation of the fluid within the testing tube. In the absence of

axial pumping or its ineffective operation, there is a restricted fluid interchange between the high shear area (located between the blade and the vessel wall) and the low shear region (within the inner edge of the blade). This is stressed out in the case of vane and cylindrical spindles. For instance, despite producing similar levels of deformation as a helical ribbon impeller of the same diameter, their performance is inferior. This is linked to the fact that they only generate tangential flow, lacking the pumping action required to create fluid circulation within the vessel. Fig. 2.2 on the left provides a section view of the primary circulation flow in the vertical plane. As noted in [35] shear mixing primarily occurs in the gap between the blades and the wall.

The liquid that exits this gap is effectively distributed to the circulation path between the blades by the primary flow. This zone is indicated by A in Fig. 2.2**.** The secondary flow, induced by the impeller, plays a role in deforming the primary flow and enhancing the exchange of fluid between regions A and B. The presence of the side wall inhibits the secondary flow, but this effect diminishes as the clearance between the blades and the vessel wall increases. When using geometries with narrowest clearance, the secondary flow has minimal impact on the flow pattern, resulting in a gradual exchange of liquid between regions A and B. Finally, an interesting study about shape optimisation was carried out by Takahashi [34]. The authors tested several helical ribbon geometries by investigating their mixing patterns using the liquid crystal method. Thanks to that they were able to identify the best design.

In a recent study Amiraftabi [36] investigated experimentally the performance of a dual helical ribbon impeller in a gassed stirred tank reactor filled with a shear-thinning polymer. The study outlined the role of a helical ribbon impeller on mixing performance and cost of operation of a gassed stirred tank by exploring the impact of the impeller rotational speed, gas flow rate, viscosity, and clearance to the bottom on power uptake and mixing time.

2.3. Numerical studies

Experimental studies, while useful in providing real-world information, have limitations when it comes to understanding the physic mechanism behind the mixing processes. Computational Fluid Dynamics (CFD) simulations provide a greater insight to better understanding the mixing processes. Over the past few decades, simulation techniques have been widely utilised to improve mixer's design and gain better understanding of the intricate flow patterns that arise from the interaction between the impeller and the vessel wall. These simulations have proven valuable in understanding the complex fluid dynamics involved in mixing processes and have contributed to the development of improved mixer designs [26,37]. A significant contribution to the understanding of mixing performance in cylindrical vessels with helical ribbon impellers was made by Tanguy [29]. This work involved the development of a 3D model, experimentally validated. This research significantly advanced the understanding of the mixing process and provided valuable insights into the performance of helical ribbon impellers in cylindrical vessels. In their study, authors observed that at low impeller speeds (10 Rpm), there was effective liquid circulation within the vessel. However, they also found evidence of poor pumping at the bottom of the vessel, indicating limitations in fluid movement in that region. De la Villeon [38] following the study of Tanguy compared three helical ribbon impellers with different geometry. Various criteria were employed to assess the mixing effectiveness of three helical ribbon impellers installed in an industrial batch tank. All of these criteria consistently reached the same conclusion, indicating that the double helical ribbon impellers exhibit higher efficiency compared to the addition of a central screw, particularly for the shear-thinning polymer studied. Lo Presti [15] used a CFD model to reproduce an experimental campaign of viscosity measurements of heterogeneous bituminous binders using a dual helical impeller. The numerical modeling of mixing in stirred tanks has gained significant traction in recent years [39–44]. A comprehensive review can be found in the work by Sommerfeld [45]. This review provides valuable insights into the advancements and methodologies employed in CFD modeling for understanding and analyzing mixing phenomena in stirred tanks. Additionally, studies such as [46] have highlighted the significant role of CFD in advancing the understanding of mixing phenomena in stirred tanks. CFD studies were also carried out to optimize the shape of the helical impeller, finding some critical ratio that must be taken in consideration in the design of a mixer with such configuration. Tsui [37] investigated the flow mixing generated by a single helical ribbon impeller in a highly viscous fluid and provided a range of optimized parameters.

He identifies that in the design of a helical mixer impeller the parameters that must be considered to properly project a mixing device are:

- The clearance between the vessel wall and the impeller blades, c
- The impeller pitch, S
- The impeller diameter, d
- The blade width, W

with D being the diameter of the vessel.

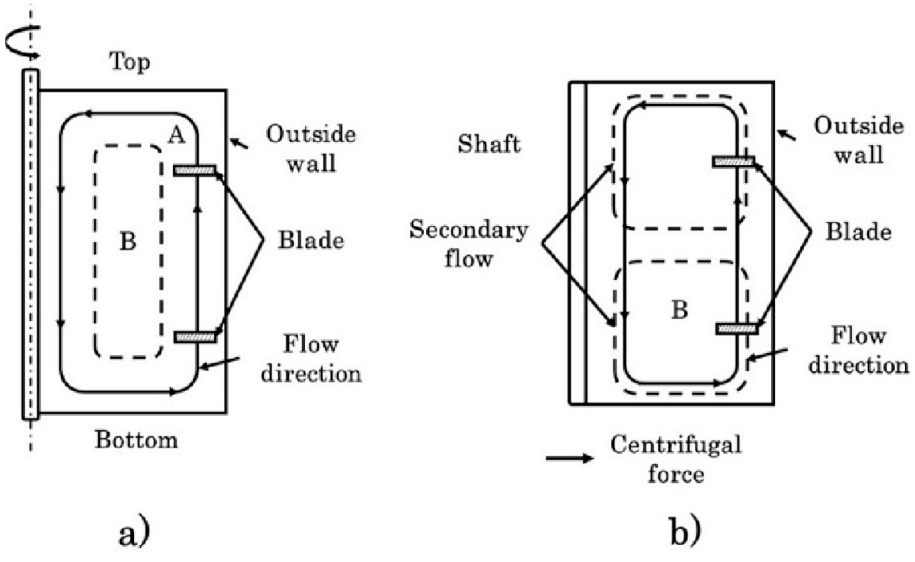

Fig. 2.2. Schematics of (a) the illuminated zone and (b) the secondary flow in a Helical Ribbon Impeller [34].

The circulation time t_c is a parameter to evaluate the mixing efficiency and is defined as the time taken for a fluid element to complete a vertical circulating loop within the vessel during the mixing process. This parameter is directly linked to the impeller's axial pumping capacity. The discharge rate of the impeller can be calculated using the following equation:

$$Q_d = \frac{v_{tot}}{t_c} \tag{7}$$

where v_{tot} is the total fluid volume of the vessel. A circulation number K_Q can be defined in terms of Q_d as:

$$K_q = \frac{Q_d}{ND^3} \tag{8}$$

The impact of impeller pitch is illustrated in Fig. 2.27. The figure shows that there is a peak value of K_Q (a parameter related to impeller performance) the specific location of this peak is influenced by the geometric design. For instance, when the blade width (W) increases, the peak location shifts, as depicted in the figure. Additionally, it can be observed that the circulation number also increases with these changes in the impeller geometry.

To achieve an optimal design, it is necessary to optimize the impeller pitch. Based on the considered configurations, the pitch value should fall within the range of S = 0.7D to D. The variation of the circulation number, as depicted in Fig. 2.3, indicates that the circulating flow generated by the impeller is strongly influenced by the blade width. When the blade width is low, even small changes in W significantly impact the circulation number. However, when the blade width exceeds 0.26D, the flow rate starts to decline. This is attributed to a reduction in the open space within the central region of the vessel, causing the returning flow to extend into the channel region.

In the case studied by Tsui [37], the impeller pitch is set at $S/D = 0.5$. It can be seen in Fig. 2.3 that when the pitch is increased to $S/D = 1$, the location of maximum K_Q is decreased to $W/D = 0.21$. A better blade width in the case of a helical ribbon impeller is in the range $W = 0.2$D to 0.26D.

In conclusion, the comparison of two blade configurations is presented in (Fig. 2.4. The first configuration serves as the benchmark, featuring a pitch (S/D) of 0.5 and a width (W/D) of 0.1, while the second configuration is optimized with a pitch (S/D) of 0.7 and a width (W/D) of 0.25. The mixing index (Δ) is a parameter employed to quantify the level of mixing within a system comprising two fluids. It measures the deviation from a uniform distribution of the two fluids. Initially, at the start of the mixing process, the mixing index has a value of 1, signifying a complete absence of mixing. As the mixing progresses, the value of the mixing index decreases and approaches 0, indicating that the mixing is becoming more complete, and the two fluids are approaching a uniform distribution. A value of 0 for the mixing index signifies that the mixing process is complete, and the two fluids are thoroughly mixed. It indicates the level of homogeneity within the sample. A high value indicates a poorly mixed system.

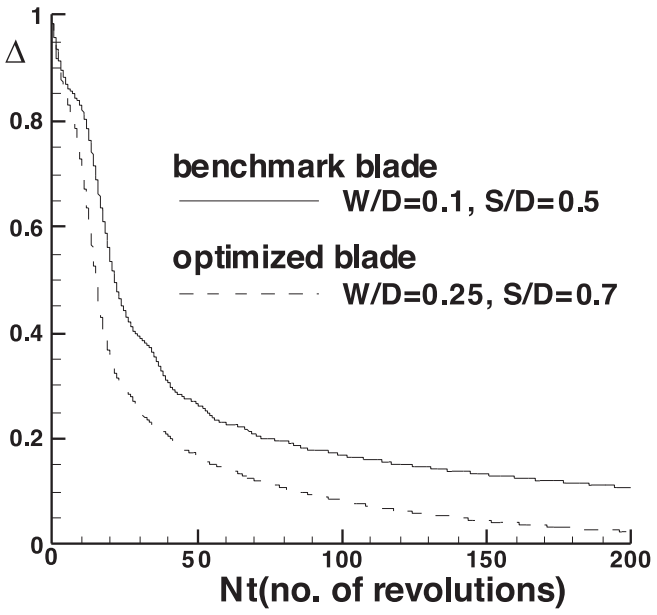

Fig. 2.4. The mixing index Δ, .
adapted from [37]

$$\Delta = \frac{P_{VOF} - \overline{C}}{\overline{C}} \tag{9}$$

here P_{VOF} is the particles volume fraction and $\overline{C}$ the mean concentration.

In a recent study [41], a dual helical ribbon impeller's performance in a shear-thinning fluid was evaluated using a combination of CFD and Population Balance Model. The study employed the standard k-ε model and Eulerian-Eulerian multiphase approach, with discrete methods for

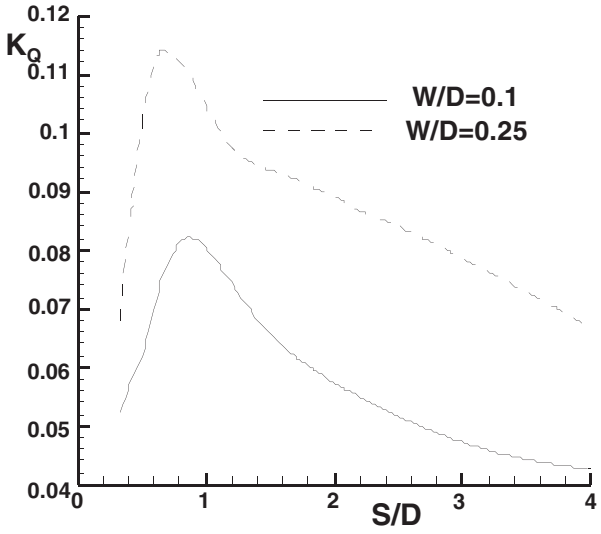

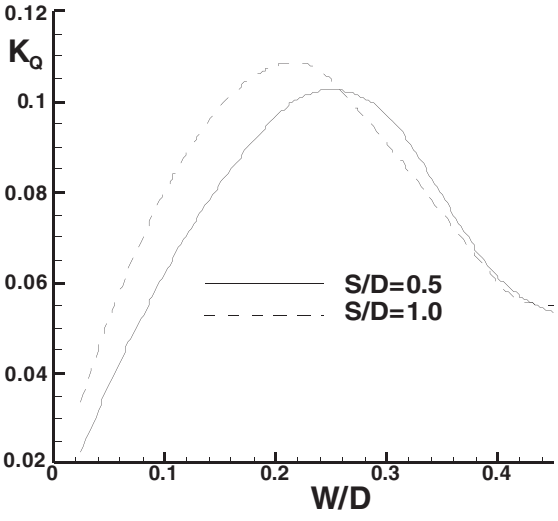

Fig. 2.3. Effects of impeller pitch blade width, .
adapted from [37]

bubble deformation prediction. Findings demonstrated that CFD results were verified against PIV tests. Delacroix [40] investigated solid–liquid mixing in the laminar regime, using a CFD-DEM model for close-clearance impellers. Among the impellers tested (anchor, double helical ribbon, Paravisc, Maxblend, and PBT), those generating high shear stress and strong bulk flow ware found to be more efficient, especially at higher viscosities. The study recommends considering these close-clearance impellers for optimal solid–liquid mixing in the laminar regime.

2.4. Calibration procedure of non-standard impeller

As extensively discussed in the preceding section, helical ribbon impellers are recognized as the most effective geometrical configurations for achieving homogenization in heterogeneous materials. These impellers like others mixing solutions are designed based on empirical or experimental correlations. In industrial applications, one of the most critical parameters during the design stage is the power consumption [28,32,47]. When mixing Newtonian fluids several studies [48,49] have shown that the correlation between the power consumption and the Reynolds number *Re* in the laminar flow is expressed as:

$$N_p Re = K_p \tag{10}$$

Here, N_P represents the power number, which is directly proportional to power consumption (P), and K_p is the power constant associated with the impeller's geometry.

In the case of Newtonian fluids, it's possible to calculate *Re* (Reynolds number) based on fluid properties and the impeller's rotational speed, from which N_P can be deduced using the power curve [50]. However, in the context of non-Newtonian fluids, viscosity varies with shear rate, introducing additional complexities. Metzner and Otto [51] extended this correlation for non-Newtonian fluids, since then their work is considered the classical approach for close-clearance impellers in industrial applications to estimate shear rates when mixing non-Newtonian fluids. They defined the apparent Reynolds number based on an apparent viscosity η_a.

$$Re_a = \frac{\rho N d^2}{\eta_a} \tag{11}$$

Where the apparent viscosity, η_a, is linked to an effective shear rate $\dot{\gamma}_{eff}$, that was assumed to be proportional to the rotational speed N as:

$$\dot{\gamma}_{eff} = K_s N \tag{12}$$

The Metzner constant, K_s, is a parameter that depends on both the geometry of the system and the flow index, n. It is used to characterize the flow behaviour and can be obtained through experimental or numerical analysis. The specific value of Ks varies for different geometries and flow conditions, and it plays a significant role in the calculation or prediction of fluid flow properties and performance. For non-Newtonian fluids the apparent viscosity η is written as:

$$\eta_a = k\dot{\gamma}_{eff}^{n-1} \tag{13}$$

In this context, 'k' represents the consistency index, which is linked to the viscosity of the fluid at 1 s^{-1}, and 'n' stands for the flow index, indicating how the fluid behavior deviates from the Newtonian model. Tanguy [29] demonstrated a strong correlation between the power curve of non-Newtonian fluids obtained using the Metzner-Otto method and that of Newtonian fluids. This reaffirms why the Metzner-Otto approach is well-recognized for designing impellers for non-Newtonian fluids.

The coefficient ' K_s ' can be determined experimentally through either the Metzner-Otto method or the Rieger-Novak method [49,52]. By following the Metzner method, the values of Re_n and Kp_n can be expressed as follows:

$$K_{pn} = N_p Re_n = K_p K_s^{n-1} \tag{14}$$

where K_{pn}, defined as the power constant for non-Newtonian fluids, is a function of n [47]:

$$K_s = \left(\frac{K_p(n)}{K_p}\right)^{\frac{1}{n-1}} \tag{15}$$

The approaches here introduced are founded on the Metzner and Otto concept and both allow to obtain K_s by measuring the power input of mixing device. The reasons of doing that lays in the fact that these concepts can be translated to any torque measurement device, such as a rotational viscometer.

2.5. Optimised design: The dual helical ribbon (DHR)

Following an extensive investigation of various mixing devices in the literature, it was revealed that the dual helical ribbon (DHR) impeller stands out as the most effective solution among close-clearance impellers for mixing highly heterogeneous fluids. This design significantly diminishes the heterogeneity of the test sample by generating an axial flow, enabling the continuous replacement of fluid within the measurement chamber. This attribute contributes to achieving more consistent and representative viscosity measurements. The optimal geometrical ratios for this mixing process have been identified as follows:

$c/D = 0.06$, $s/D = 0.9$, $w/D = 0.15$,

where, c is the clearance between blades and wall, D the diameter of measuring chamber (19 mm), while d, s and w are respectively the diameter, the pitch and width of the impeller.

3. Design & manufacturing

3.1. Computational fluid dynamics modelling

A CFD analysis was carried out to design and validate the new geometry. For instance, due to the high manufacturing cost the use of the computational platform helped to avoid a trial-and-error process that could had turn in a costly and time-consuming procedure. Indeed, the numerical modelling provided useful evidence about the device performance that allowed to proceed to the manufacturing of the DHR with relatively confidence.

3.2. CFD model set-up

Version 20 of Ansys Fluent was used in this study [53]. The software allows to solve a wide range of fluid flow problems, such as laminar non-Newtonian flows in process equipment and multiphase flows [53], to name but a few. During the set-up of a numerical model, the main stages to define are:

- CAD creation
- Meshing
- Selection of a physical model
  - Viscous model
  - Multiphase model
- Materials
- Boundary conditions
- Solution

ANSYS was used to produce a CAD model of the DHR and then a mesh (Fig. 3.1), which consists in about 150,000 cells. The numerical study also included the simulation of a coaxial cylinder, specifically the spindle SC-27. The purpose of this was to compare the DHR with the most widely used device for rotational viscosity testing and to gain insight into phenomena such as phase separation, sedimentation, etc. A

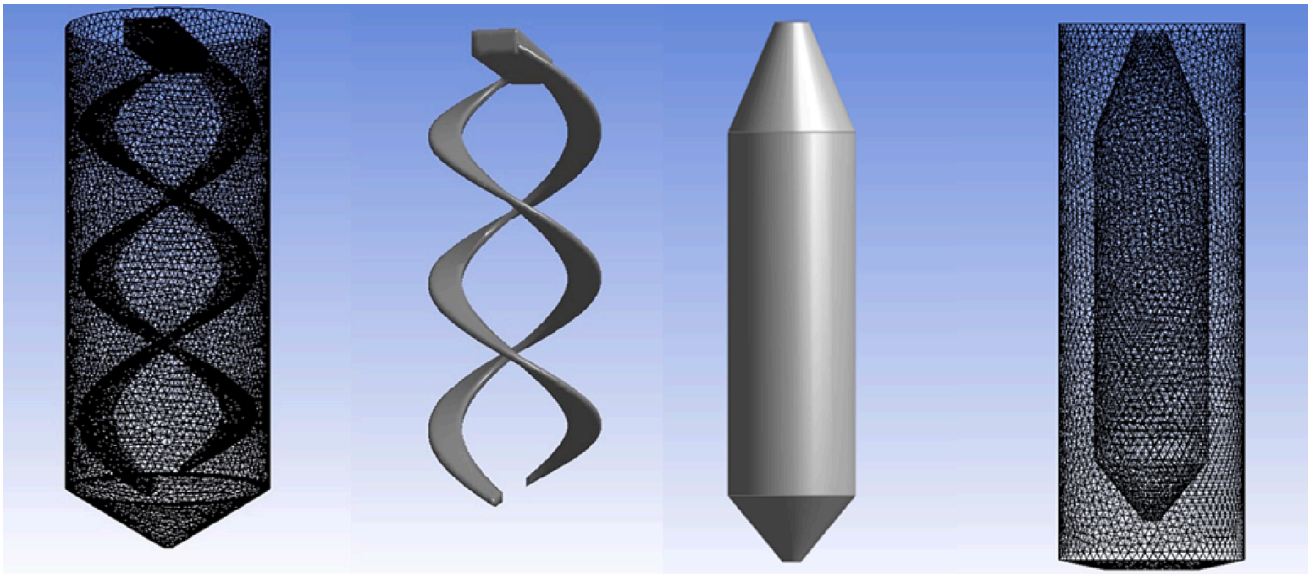

Fig. 3.1. The surface mesh and a solid model of the DHR (left) and SC-27 (right).

similar process was used to produce a mesh of 110,000 cells (in the inflation layers adjacent to walls) for the SC-27 spindle (Fig. 3.1). To address the step variations in flow variables near the container wall caused by the no-slip condition, inflation layers were introduced near the wall. This approach improves the accuracy of predicting flow variables in this region. To ensure the reliability of the simulations, a mesh-independence study was conducted. This involved performing multiple simulations using different mesh sizes, starting with a coarse mesh and gradually refining it. The study aimed to determine the point at which the results became independent of the mesh size, ensuring that the simulation outcomes were not influenced by the chosen mesh resolution.

Analysis of the velocity field in crucial areas of the domain showed that the mesh with 150,000 elements for the DHR and 110,000 for the SC-27 was sufficient for this analysis, since the meshes with more elements lead to a very similar result with the accompanying increased computational effort. For mixing vessels is common to use the mixing Reynolds number, Re_a to describe the flow (Equation 11). In this investigation, the mixing Reynolds number was below 100, assuming laminar flow conditions for all simulations, therefore the laminar model was selected, and particles included by defining the diameter (400 μm) and the concentration (5 %). Subsequently, the rotational speed was configured within the range of 0 to 200 Rpm. In both geometries, the upper boundary conditions were defined as a symmetry plane since the shear interaction between air and bitumen was not significant. Furthermore, no-slip wall boundary conditions were implemented to replicate the fluid's movement along the inner walls of the geometry. To reproduce the rotation of the impellers, a maximum angular change of 2° was allowed per time-step. To clarify, if the impellers are rotating at a speed of 100 Rpm (revolutions per minute), this translates to 1 revolution every 0.6 s. Since 1 revolution corresponds to 360°, the impellers require 180-time steps to complete a full revolution (as each time step covers 2°). Therefore, to accurately capture the impeller motion, a time step of 0.6/180 = 0.00333 s is needed. This ensures that the simulation accurately represents the rotational behavior of the impellers with the desired level of temporal resolution.

3.3. Kinematic similarity

Once that the CFD model was setup, an initial study was carried out to test the DHR design for kinematic similarity. In the field of fluid mechanics, Kinematic similarity in fluid mechanics refers to maintaining the same flow streamline shape while scaling the velocity at corresponding points in the model and prototype flows. This is achieved by applying a constant scale factor to ensure proportionality between velocities. Kinematic similarity allows researchers to study prototype flows based on scaled-down models, enabling valuable insights and predictions for real-world applications [54]. The idea behind these tests was to prove that increasing the rotational speeds the flow pattern was not affected by the shear rate applied. For both a Newtonian (Visco-FluidF100) and a non-Newtonian (Xantana 0.25 %) fluid, the model was run at 10, 50, 100 and 200 Rpm and components of the velocity were analysed along two lines through the domain – a vertical line going from the bottom to the top along the centre line of the vessel and a horizontal one in the middle of the sample. By using an appropriate non-dimensionalisation, where the normalisation is the component of velocity (u, v or w) divided by ωD (s^{-1}•m) (the angular velocity multiplied by the diameter of the vessel, Fig. 3.2 and Fig. 3.3 depict the variations of the scaled w and u components of velocity. These components are defined as the portions of the velocity aligned with the coordinate system vectors along these two lines, for both Newtonian and non-Newtonian fluids. In Fig. 3.2, it is observed that, along a vertical line running through the center of the device, the flow moves vertically upward, creating a motion capable of transporting particles from the bottom to the top of the vessel. The convergence of lines for the Newtonian fluid suggests kinematic scaling. In the case of non-Newtonian fluids, there is some variation, confirming the shear-thinning properties of the fluid. Contrastingly, Fig. 3.3 depicts the x-component of the velocity on a horizontal centreline. This flow pattern is characteristic of a rotating body of fluid—accelerating as we move away from the center of rotation, only slowing down as it approaches the gap between the impeller and the wall, experiencing the effects of wall friction. The y-component exhibits a nearly identical pattern. The fact that non-Newtonian fluids produce a lower normalized velocity and a smoother one, confirms the markedly different viscosity observed in these fluids when compared to Newtonian fluids. What the two figures show is that, over a wide range of rotational speeds, the flow within the vessel displays kinematic similarity – the flow patterns seen are apparently independent of the shear rate and the properties of the fluid. This gives us confidence that the DHR design can be used as a viscometer across a range of shear rates. If these velocity profiles differed over a range of shear rates, then the device would effectively have different flow patterns at different speeds and any extrapolation of results at one shear rate would be impossible.

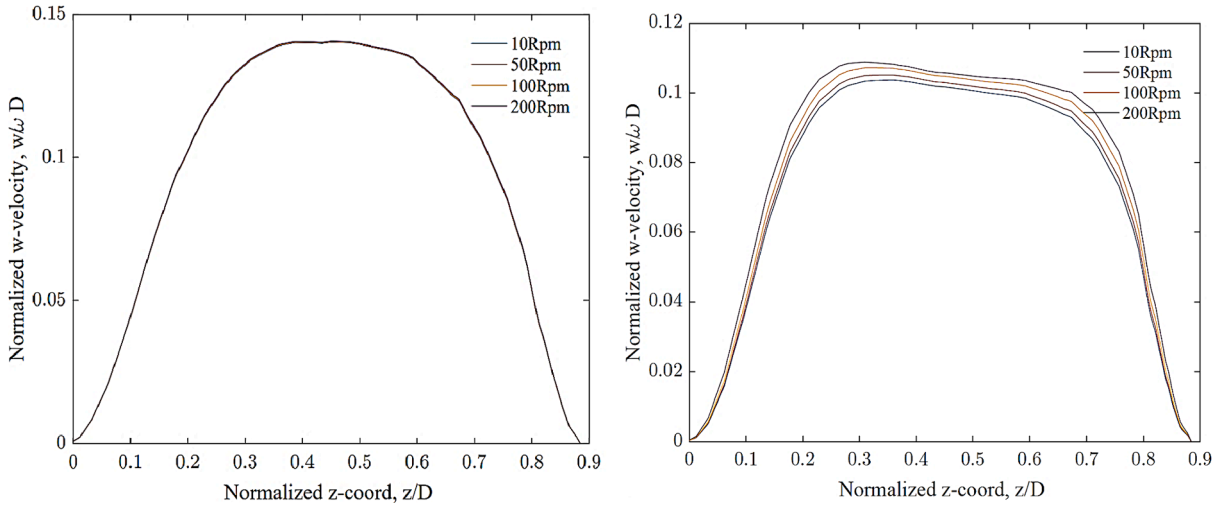

Fig. 3.2. Plots of the non-dimensional w-component of velocity along a vertical centreline, from bottom to top, for the Newtonian fluids (left) and non-Newtonian (right) developed by using the Dual Helical Ribbon.

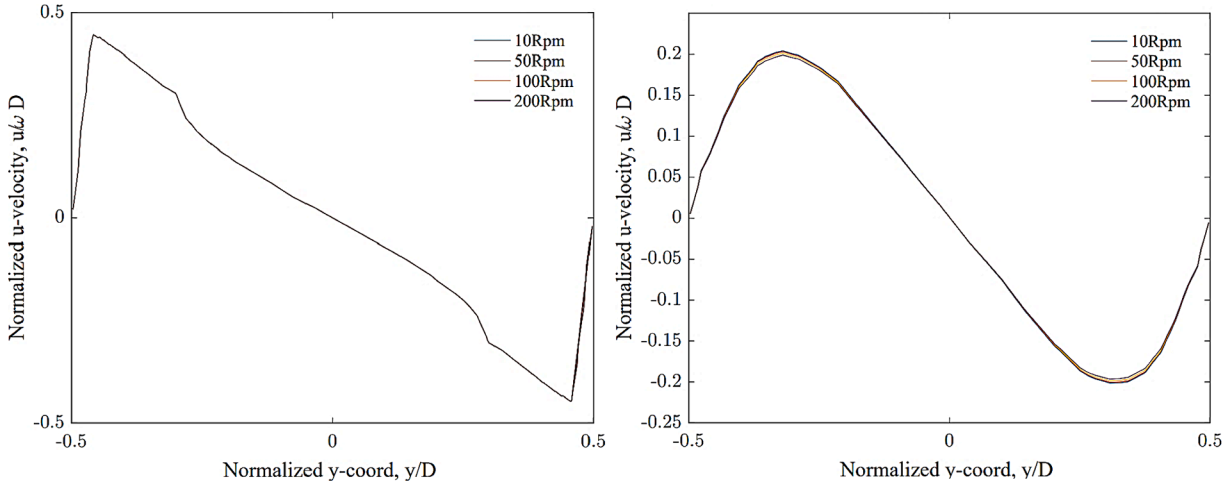

Fig. 3.3. Plots of the non-dimensional u-component of velocity along a horizontal centreline for the Newtonian fluids (left) and non-Newtonian (right) developed by using the Dual Helical Ribbon.

3.4. Multiphase simulations

With confidence in the kinematic similarity gained from the previous section, multiphase simulations, using the mixture model as previously described, were run to investigate the mixing of rubber particles in the DHR. Various Newtonian fluids were tested; 5 % by volume of rubber particles were used with a diameter of 400 μm and density of 1050 kg/m^3; and different rotational speeds (10, 50, 100 and 200 Rpm) were selected. In addition, several non-Buoyant cases were run where the density of the rubber particles exactly matched the density of the background Newtonian fluid as specified in Table 3.1. As mentioned in the previous section, a useful measure of the mixing within the vessel is the mixing index.

Table 3
K_s and K_p values calculated in this work for each n.

n	K_p	K_s
0.69	41	537
0.37	8	292
0.30	10	130
0.21	22	26

Table 3.1
Fluids and particle properties.

	Fluid		Particles		
Name	Density (kg/m^3)	Viscosity (Pa·S)	Diameter (μm)	Volume fraction	Density (kg/m^3)
f10	940	0.01			
f100	960	0.1	400	5 %	1050
f500	970	0.5			

Fig. 3.4 shows the variation of the mixing index with the mixing Reynolds number for both buoyant and neutrally buoyant particles. We see that for the neutrally buoyant particles, the mixing index is independent of Reynold number because the particles do not tend to settle out and the mixing is sufficient to keep them well mixed at any rotational speed. However, for the f100 fluid shown, there is a clear decrease in the mixing (as witness by an increase in the mixing index) for buoyant particles at the lowest rotational speed. For the higher two of the four speeds used, the mixing index becomes uniform, but at the lower speeds it increases. This has implications for the use of the DHR as a viscometer because of this dependence on the mixing Reynolds number. However, the deviation of volume fraction from the mean in all these cases is very

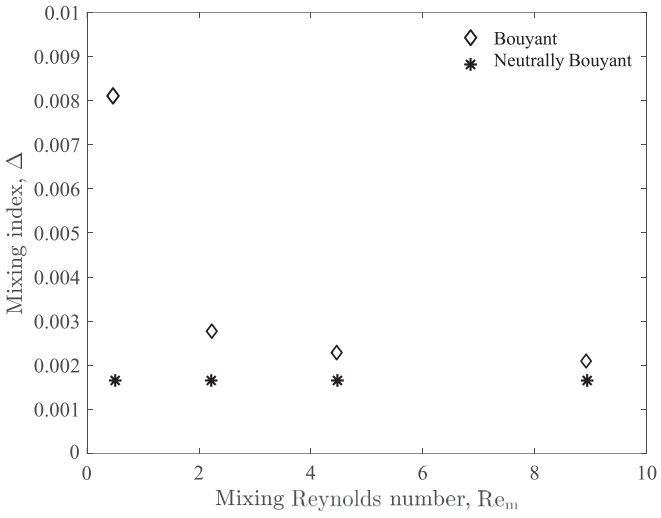

Fig. 3.4. Plot of the mixing index, Δ, against mixing Reynolds number, Rem, for the f100 fluid with 5% rubber particles (both buoyant and neutrally buoyant).

small. Indeed, just how comparatively small the mixing index is for the DHR can be highlighted when the mixing capability of the DHR is compared with the SC-27 under identical conditions.

Fig. 3.5 illustrates the relationship between mixing index, rotational speed, and fluid for both the SC-27 and DHR impellers. It can be observed that all devices produce more homogeneous mixtures at higher rotational speeds. However, the mixing index for the SC-27 under all conditions produced a highly stratified mixture, while the DHR does not. It is worth noting that the y-axis is logarithmic. These findings are further emphasized by Fig. 3.6, which shows contours of particle volume fraction and velocity from both the SC-27 and DHR simulations. It is evident that there is a stratification of the particles in the SC-27 model, while the DHR model displays a near-homogeneous value for the volume fraction. In summary, the velocity magnitude plot for the SC-27 shows that once a particle has settled towards the bottom of the vessel, there is no mechanism for it to be re-entrained in the flow due to the low velocities outside of the zone between the two cylindrical surfaces. On the other hand, the DHR configuration appears to have an upward flow of fluid that is sufficient to re-entrain the particles in the similar zone

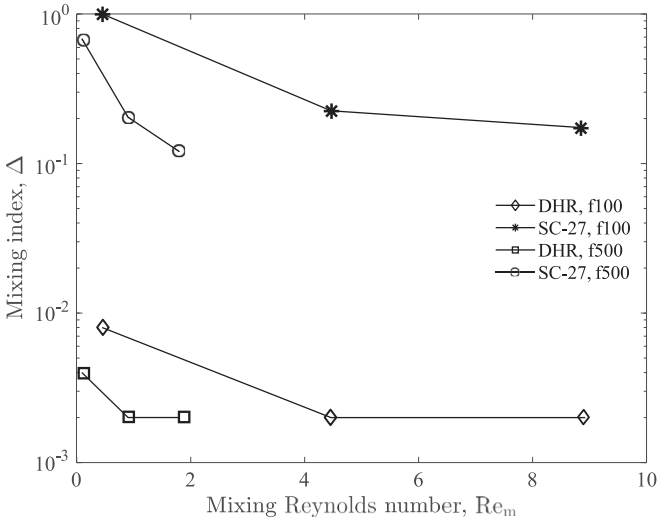

Fig. 3.5. Plot of the mixing index, Δ, against mixing Reynolds number, Rem, for the f100 and f500 fluids with 5% rubber particles for the DHR and SC-27 impellers.

towards the bottom.

3.5. Manufacturing process

The numerical analysis proved that the DHR design worked as intended. However, before proceeding to manufacture the part in stainless steel, the DHR was realised by using the 3D printing technology. Thanks to this innovative technique it was possible to reduce manufacturing time and costs but also to make different prototypes to achieve the final geometry. A Stratasys Dimension 1200es powered by Fused Deposition Modelling (FDM) technology was used. The part was printed in real Acrylonitrile Butadiene Styrene (ABS) thermoplastic, material that during the tests showed to be affordable, but also durable. Finally, the set of DHRs was printed and adapted to a Brookfield rotational viscometer model LVDV-II + Pro EXTRA.

At this stage, the author wanted to evaluate the mixing performance of the DHR by visual assessment. To provide the reader with further details the validation process was performed by comparing the DHR also with the DHI previously introduced. Tests were performed by adapting the DHR and DHI on the rotational viscometer. Nine fluids made up from the combination of different fluids and crumb rubber particles concentrations (1, 3 and 5 %) were evaluated (Table 3.1). All the tests have been carried out at 10, 50 and 100 Rpm.

A glass tube in place of the conventional one allowed a visual investigation aimed to assess the mixing performance of each geometry. Indeed, thanks to the transparent fluid it was possible to visualise the mixing between the fluid (transparent) and the particles (black). Table 3.2 summarizes if the selected impeller is able to keep the particles suspended within the sample (O) or not (X). Furthermore, in the table the symbol (-) reports if the reading exceeds the lower or higher limits of the viscometer. Results proved that the DHR extends the range of measurements while respecting the limits recommended by the ASTM standard.

The device was constructed from stainless (Fig. 3.7) steel at the Precision Manufacturing Centre located within the University of Nottingham. Furthermore, the authors made a deliberate decision to produce a series of DHR models, specifically DHR 1.0, DHR 2.0, and DHR 3.0, to enhance its versatility and expand its range capabilities (Fig. 3.8). By increasing the pitch of the DHR, it became possible to reduce the torque required by the viscometer, thereby extending the scope of viscosity measurements. The calibration process for the DHR involved the utilization of a wide range of Newtonian and non-Newtonian fluids. This calibration procedure took place at the Laboratory of Complex Fluids, situated at the University of Huelva.

4. Calibration procedure

If the DHR is to be used to measure the behaviour of heterogeneous materials, some of which may be non-Newtonian, it is important to calibrate the new design against a range of non-Newtonian fluids. Here we use the Rieger-Novak approach as an alternative method to the classical Metzner and Otto.

4.1. Materials

The first step of the calibration procedure was to prepare the materials necessary to carry out the experimental campaign. Five materials (Table 4.1) were selected to cover the wider range possible of flow index. A low shear mixer was used to prepare the systems, to obtain stables mixtures the mixing time required was about 12 h for each system.

4.2. Rheological measurements - parallel and plate

Rheological tests (parallel and plate) were carried out by using a Malvern Kinexus PRO to obtain values of shear stress, τ, determined from the torque applied to the sample, at a number of shear rates,$\dot{\gamma}$,

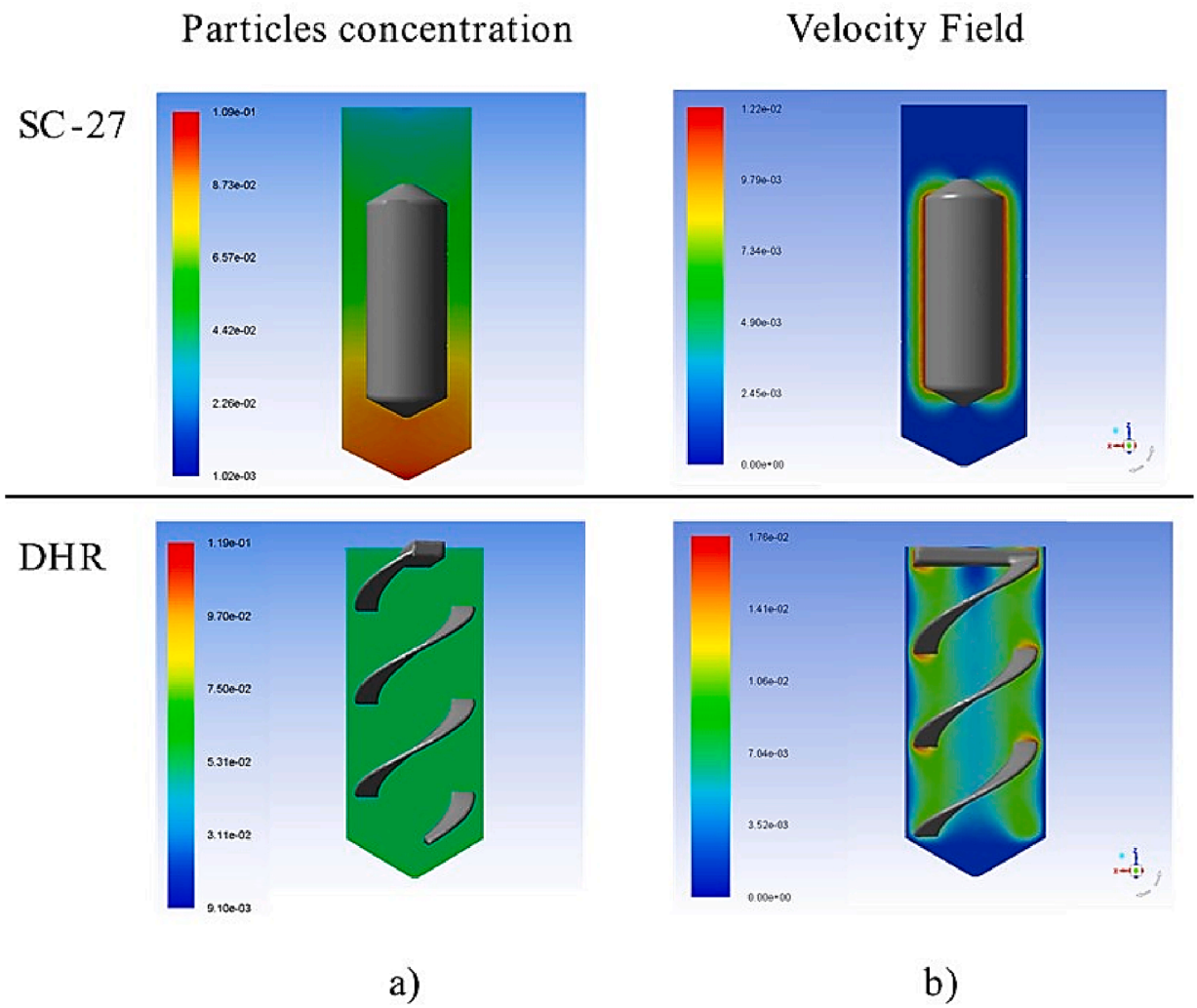

Fig 3.6. Contours of (a) volume fraction and (b) velocity magnitude of f100 + 5 % particles at 20 Rpm.

Table 3.2
Rotational test results comparison between DHI and DHR, where (o) indicates cases where the geometry was able to keep the particles suspended within the sample, (x) not and (-) reports if the reading exceeds the lower or higher limits of the viscometer.

Fluids	DHI			DHR		
	10 Rpm	50 Rpm	100 Rpm	10 Rpm	50 Rpm	100 Rpm
f10 1 % CRM	X	X	O	O	O	O
f10 3 % CRM	X	X	O	O	O	O
f10 5 % CRM	X	X	O	O	O	O
f100 1 % CRM	O	O	–	O	O	O
f100 3 % CRM	O	O	O	O	O	O
f100 5 % CRM	X	O	O	O	O	O
f500 1 % CRM	O	O	–	O	O	O
f500 3 % CRM	O	O	–	O	O	O
f500 5 % CRM	X	O	–	O	O	O

determined from the angular velocity of the plates.

For the non-Newtonian materials, a power law was assumed according to Equation 13. Tests were performed for each material by using a parallel and plate configuration with a diameter of 35 mm; operating parameters are showed in Table 4.2, to find out the consistency index k and the flow index n, that are respectively a measure of the average viscosity of the fluid and an indication of the deviation from Newtonian behaviour.

Indeed,

$$n\begin{cases} < 1 Shearthinning(pseudoplastics) \\ = 1 Newtonianfluid \\ > 1 Shearthickening(dilatantfluids) \end{cases}$$

Taking logarithms of both sides of equation 13 gives:

$$log_{10}\eta_a = (n-1)log_{10}\dot{\gamma} + log_{10}k \tag{18}$$

The fittings curves of Equation 18 are shown in Fig. 4.1 for each of the five fluids tested in this way. The Newtonian visco-fluid has a flow behaviour index of close to unity, as expected, while all the other fluids have a value of less than unity, indicating that they are shear-thinning.

It was key at this stage to have as large a range of values of n for subsequent testing of the DHR design. Each fluid showed a trend as in Fig. 4.1, then it was assumed that every fluid was a power law fluid. The two key parameters n and k are respectively the slope and the intercept and are gathered in Table 4.1. Results proved that the flow index calculated covered a satisfactory range of the shear thinning behaviour fluids (n in the range 0.2–0.7).

Fig. 3.7. DHR solid model (left), 3D printed prototype (centre) and stainless steel (right).

Fig. 3.8. The DHR set, DHR 1.0 on the left, DHR 2.0 on the centre and DHR 3.0 on the right.

Table 4.1
Values of n and k for each system used in this study (equation 18).

Fluid	Flow index - n	Consistency index - k
1 % Xanthan Gum	0.2	28.1
0.5 % Xanthan Gum + 0.5 % Guar Gum	0.3	38.6
0.25 % Xanthan Gum	0.4	6.4
1.5 % Xanthan Gum + 3 % CMS*	0.69	6.4
Visco-fluid	0.99	4.4

(* CMS is carboxymethylcellulose sodium salt).

4.3. Rieger Novak calibration procedure

The straightforwardness of the Rieger and Novak method is one of its key advantages. Indeed, this method aims to correlate the effective shear rate with the power draw. If the fluid rheology is described by the power law model (equation 13), a particular Reynolds number is obtained:

Table 4.2
Parameters used during parallel and plate tests.

Temperature	time	Shear rate	Geometry
30 °C	30 min	0.01 to 100 (1/s)	PP 35 mm

$$Re_{pl} = \frac{\rho N^{2-n} D^2}{k} \tag{18}$$

In this method, power input data N_P (equation 19) manipulated with Re_{pl}, Fig. 4.2 shows a family of parallel curves, with each curve corresponding to a specific value of n. To plot those curves was necessary to calculate the power number N_P:

$$N_P = \frac{P}{\rho N^3 D^5} \tag{19}$$

Where ρ is the material density, N the rotational impeller speed D the viscometer tube diameter and P the viscometer power consumption, defined as follow:

$$P = 2\pi N M_t \tag{20}$$

With M_t the torque recorded for each fluid investigated. To this end, the DHR was adapted to a rotational viscometer, to record for each material the trend of the torque as a function of rotational speed (0 to 200 Rpm at 30 °C for about 30 min).

Based on Equation 19, the experimental power input for each shear thinning fluid listed in Table 4.1 is plotted against the power-law Reynolds number, Repl, defined by Equation 18. In correlation with the Reynolds number, there's a decrease in power consumption as the flow behavior index *'n'* decreases. The graph further illustrates that as *'n'* approaches the critical Newtonian value ($n = 1.0$), the power data conforms to the Newtonian power relationship. Importantly, the results depicted in Fig. 4.2 enable the estimation of power constant *'Kp'* values as a function of *'n'*. This method doesn't necessitate prior knowledge of *'Ks'* values to compute power consumption. To examine the impact of shear-thinning behavior on power consumption, the concept of a characteristic velocity is employed. In accordance with Equation 19, the experimental power input for each of the shear-thinning fluids outlined in Table 4.1 is plotted against the power-law Reynolds number, Re_{pl}, as defined in Equation 18. As anticipated, power consumption diminishes

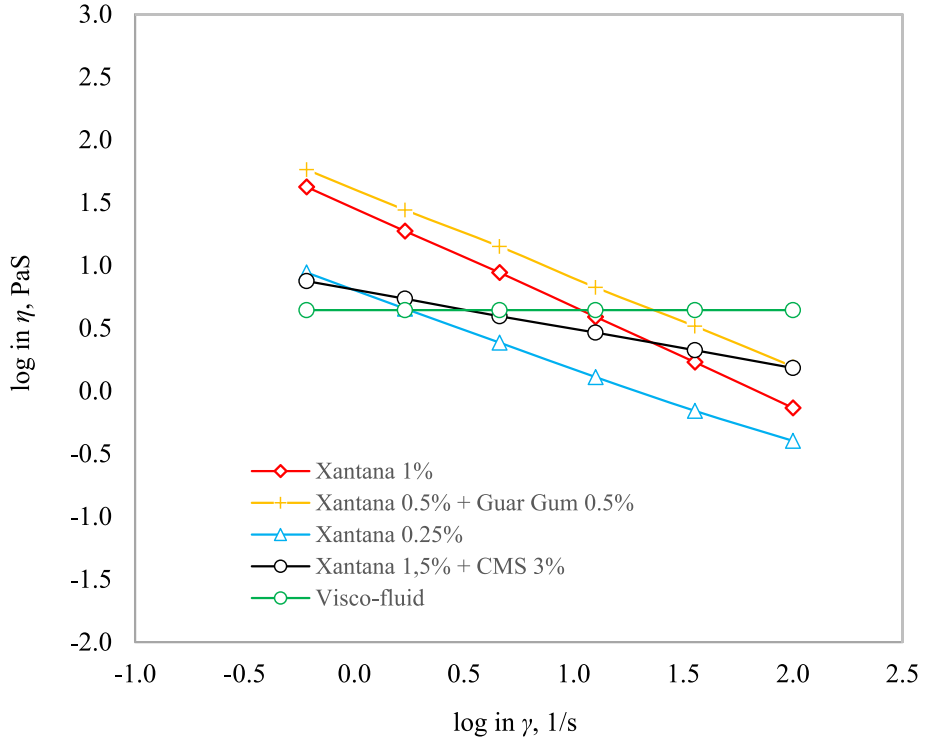

Fig. 4.1. A plot of the flow behaviours for the fluids investigated in this work.

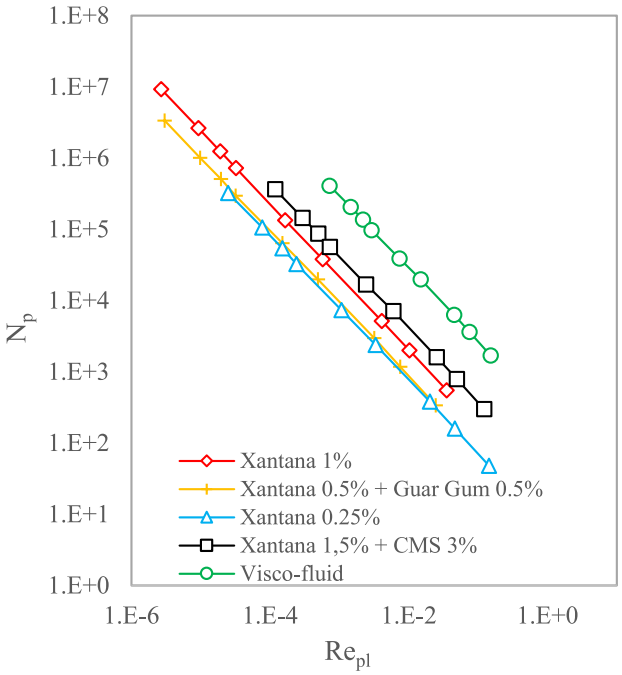

Fig. 4.2. Power consumption curve for the power law fluids of this study using the characteristic velocity approach.

with a reduction in the flow behavior index, denoted as *'n,'* while maintaining the same Reynolds number. The graph also illustrates that as *'n'* approaches the ultimate Newtonian value ($n = 1.0$), the power data tends to align with the Newtonian power correlation. It's worth mentioning that the results depicted in Fig. 4.2 enable the calculation of the power constant, *Kp*, values as a function of 'n.' In this method, there's no requirement for prior knowledge of *Ks* values to compute power consumption. However, if a conventional dimensionless representation of power data (*Np* vs. *Re*) is desired, then knowledge of *Ks* values becomes essential. Combining equations 17 and 18, it is understood that the power constants for Newtonian (*Kp*) and non-Newtonian fluids (*Kp*(*n*)) are respectively defined as:

$K_p = N_p Re_a$ (21)
$K_{p(n)} = N_p Re_{pl}$ (22)

it is straightforward to show that:

$$P = K_p \eta_a N^2 D^3 \tag{23}$$

By using the Metzner & Otto method, the power number becomes N_p, becomes:

$$N_p = \frac{K_p K_s^{n-1}}{Re_{pl}} \tag{24}$$

Using equation 22 we get:

$$K_s = \left(\frac{K_p(n)}{K_p}\right)^{\frac{1}{n-1}} \tag{25}$$

where K_p for DHR had a value of 290.

Ultimately, to achieve a non-dimensional and distinct portrayal of the power input, the experimental data, dependent on the apparent Reynolds number as defined in equation 11, is recalibrated by employing the Ks(n) values provided in Table 3. As can be seen from Fig. 4.3, the whole power draw data, including those for the Newtonian fluid, are brought together into a single dimensionless function. To describe the relationship between K_s and the flow index n the following nonlinear regression was adopted:

$$K_s = ab^{n-1}c^{\frac{n-1}{n}} \tag{26}$$

The model defined by equation 26 fits the experimental $K_s(n)$ values for n quite well ranging from 0.2 to 0.8. It must be noted that to increase the reliability of the model the number of materials investigated might be extended.

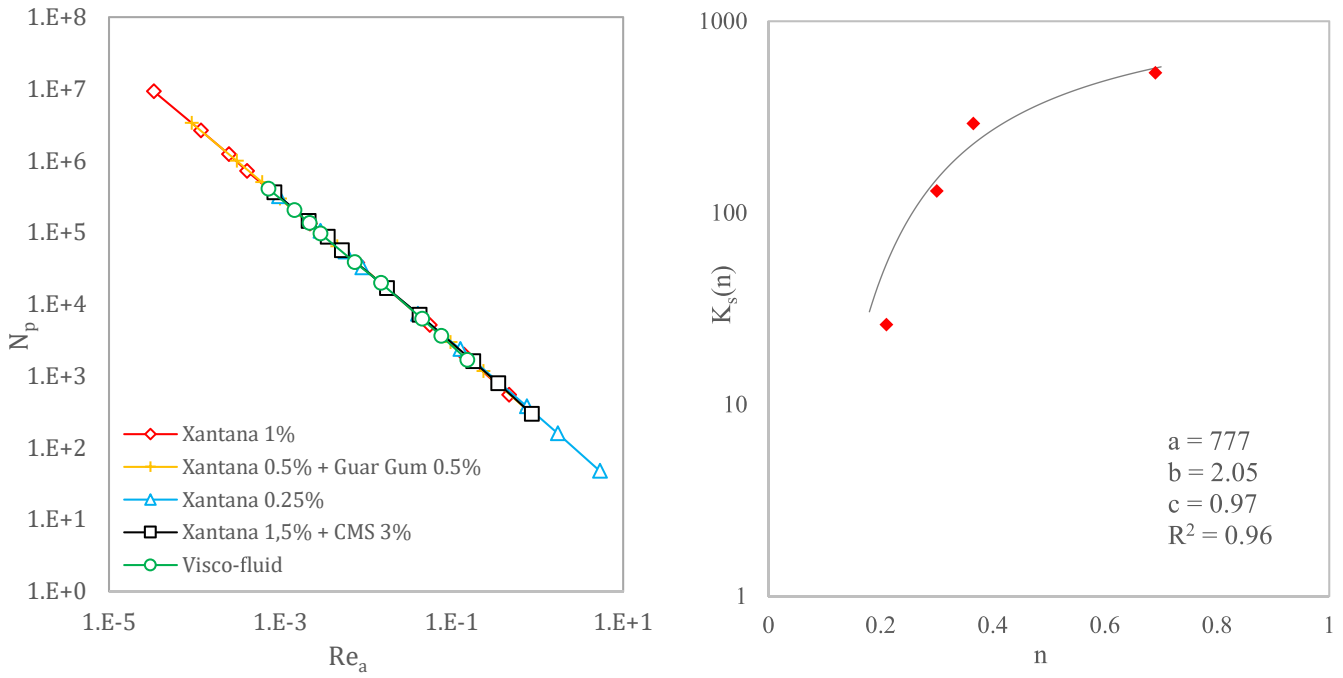

Fig. 4.3. Generalized dimensionless power consumption curve for the DHR (left), K_s as a function of the flow behaviour index, n. $K_s(n)$ is given by equation (26).

At this stage the calibration procedure was completed and a master curve no matter the *n* value considered was obtained. Finally, combining equation 19, 20 and 24, we get calibration following equations,

$$\eta_a = \frac{2\pi M_t}{K_p N D^3} \tag{27}$$

$$\dot{\gamma}_a = K_s N \tag{28}$$

As a result, these equations would allow DHR to measured Newtonian and non-Newtonian viscous behaviour of complex (heterogenous) fluids. However, the K_s parameter, unlike the SRC parameter used in Equation 6, are not constant for a selected geometry or sensor system. Ks and calculated average shear rate depend on the shear-thinning behaviour of the tested non-Newtonian fluid (specifically, on its Power Law 'n' flow index). This is demonstrated by combining Equations 26 and 28:

$$\dot{\gamma}_a = 777\hat{A}\cdot 2.05^{n-1} 0.97^{\frac{n-1}{n}} N \tag{29}$$

Although this fact may be relevant for the practical determination of the average shear rate, it is worth noting that the 'n' value of the tested fluid can be easily calculated using raw data (torque values, Mt, and rotational speeds, N) recorded during its steady flow test. The parameter 'n' is obtained from a log–log plot of the fluid apparent viscosity, obtained from Equation 27, versus the applied rotational speed, N. As a result, this method provides a feasible and objective evaluation of the fluid characteristics.

5. DHR validation

5.1. DHR as testing geometry for rotational viscosity measurement of highly heterogenous fluids

A series of multiphase fluids were created by combining different Newtonian fluids (Brookfield standard fluids) and crumb rubber particles (refer to Table 3.1). The particles were introduced into the fluid, and the mixture was subjected to agitation to achieve a uniform dispersion of the particles throughout the fluid. Subsequently, these fluids underwent testing in a Brookfield DV-II PRO Digital Viscometer, utilizing the SC-27 and DHR as the testing geometries. The impellers were swiftly immersed into the blend, and the viscometer was activated to commence the test. Torque and viscosity measurements were then continuously recorded throughout the testing procedure. These were tested at various rotational speeds up to a maximum of 100 Rpm at 25 °C for period of 45 min. Each reported result is obtained as an average of at least three repetitions under the same experimental conditions.

It is noted that the viscosity of a dilute suspension can be found from the Einstein equation.

$$\eta = \eta_0(1 + 2.5\phi) \tag{30}$$

where η_0 is viscosity of the background fluid and ϕ is the dispersed phase volume fraction (with a requirement that $\phi < 0{:}1$).

Experimental tests were carried out at three distinct rotational speeds: specifically, at 10 Rpm, 50 Rpm, and 100 Rpm. These tests were designed to assess and analyse the reaction and effectiveness of the two geometries in use.

The purpose of conducting tests at multiple speeds was to examine the impact of rotational speed on the mixing process. Fig. 5.1 shows the variation of viscosity with time for both the SC-27 and DHR impellers at 10 and 100 Rpm for a 5 % mixture of rubber particles and the f10 fluid. Also shown on this and the subsequent two figures is the prediction of viscosity from Equation 5. For the SC-27 spindle, a high initial viscosity is seen at both speeds due to issues with accelerating the fluid and particles up to a constant speed. The viscosity then decreases gradually over the 45-minute testing period, falling below the Einstein viscosity in the process. This is due to the settling of the particles during the test, producing a fluid in the gap between the cylinders that is virtually free from particles Fig. 5.1 b). At 10 Rpm, the DHR provides produces more constant values of viscosity, which are also closer to the Einstein value. There is still a small decrease over the run time, but this appears to stabilize after 25 min. For the higher shear rate, the value of viscosity for the DHR is fairly constant during the test, only falling slightly towards the end. The value seen is very close to the Einstein prediction and is due to the particles remaining in suspension throughout (Fig. 5.1 d). Increasing the rotational speed produces lower values of viscosity for impeller due the shear-thinning behaviour of the fluid/particle mixture. At this point it is useful to consider the settling time, t_s, for a rubber particle in the background fluid.

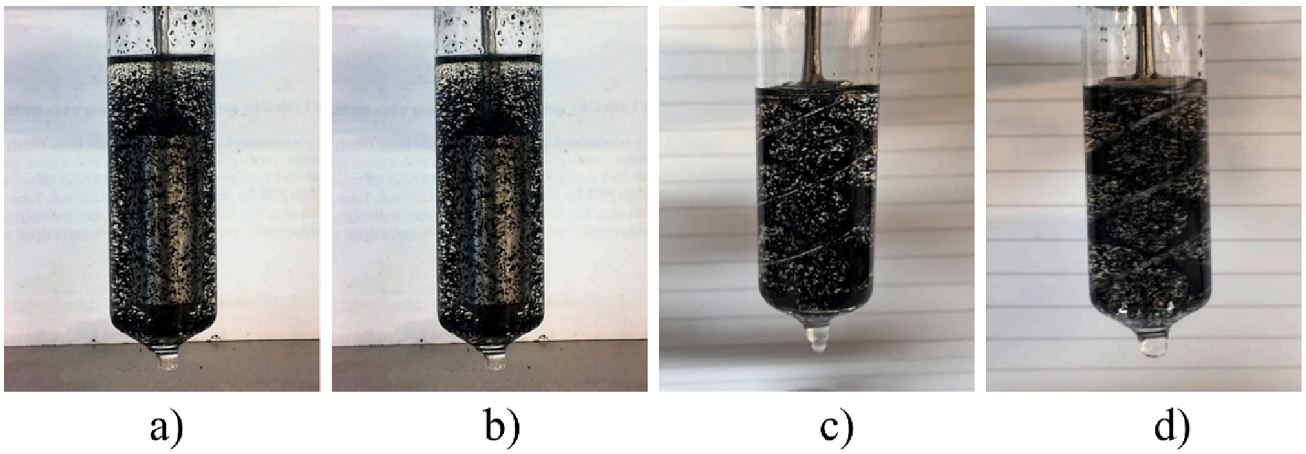

Fig. 5.1. Photographs of the SC-27 and DHR impellers with a mixture of f10 fluid and rubber particles at the start (a), (c) and end (b), (d) of the tests.

$$t_s = \frac{H}{v_t} \tag{31}$$

where H is the height of the Brookfield tube and v_t is the terminal velocity of the particles

$$v_t = \frac{(\rho_p - \rho_f) d^2{}_p g}{18\mu_f} \tag{32}$$

where ρ_p and ρ_f are the densities of the particles and fluid respectively, d_p is the diameter of the of the particles and μ_f is the viscosity of the background fluid. For the f10 fluid, we find a settling time of the order of 1 min, for f100, 10 min and 50 min for f500. These are rough values, assuming the fluid is stationary and the complete absence of other particles in the background fluid.

With this in mind, Fig. 5.2 shows the evolution of viscosity, it is clear that the SC-27 impeller in both cases shows the gradual decrease in time that was seen for the f10 fluid, albeit the decrease is slower (due to the increased settling times). For the DHR impeller, the values again decrease a little from their initial values, but the change is by no means as pronounced. Clearly with a settling time of the order of the length of the experiment for the f500 fluid, the values of viscosity for this experiment are by no means at their final value, those for the DHR show very little change over the period of measurement.

To complement those results a separate experiment where the particles were initially allowed to settle in the device before the DHR was rotated, reveal the mixing process clearly in Fig. 5.3. In image (a) of this figure, the particles are clustered near the bottom, while shortly after the start of the mixing process, a clear plume of particles is observed spiralling upwards in the centre of the device, image (b) after some time, image (c), the particles are evenly distributed throughout the device, confirming our previous observations. Consequently, the particles are evenly distributed within the container, preventing any separation of phases for the rest of the experiment. The obtained results strongly support and confirm the earlier mentioned statement that the rotational speed is a crucial factor in determining the degree of sample homogenization and the effectiveness of the impeller. This phenomenon directly influences the recorded viscosity values and is subject to factors such as the testing setup, rotational speed, and applied torque. The research findings suggest that changes in the rotational speed of the Dynamic Shear Rheometer (DHR) have a less pronounced impact on apparent viscosity measurements compared to the SC-27 spindle. This implies that the DHR may offer more consistent and dependable viscosity measurements across varying rotational speeds in contrast to the SC-27 spindle.

The alignment of results obtained with the DHR further substantiates earlier observations regarding the influence of rotational speed on the uniformity of the mixture. Higher rotational speeds tend to result in a more homogenous blend. However, at 10 Rpm, the viscosity measurements exhibit intermittent behavior, indicating that the particles have not yet achieved a stable distribution. Nevertheless, both the temporal viscosity values and the shear dependency analysis emphasize the advantages of employing the DHR, as it furnishes more stable and trustworthy rheological insights for this heterogeneous system. The DHR offers a favourable perspective in terms of obtaining consistent and accurate rheological data for such samples.

6. Discussion, conclusions and future recommendations

This study presents the authors' experience with using a DHR as impeller for rotational viscosity measurements of highly heterogeneous fluids, as well as the technical details required to allow material scientist to develop their own version. DHR is used for overcoming sample stability issues while testing highly heterogeneous fluids (multiphase, non-Newtonian or a combination of both) and leads to enhanced and more realistic measurements. For this purpose, after a literature study and a numerical validation of the mixing efficacy of the selected impeller, a DHR for rotational viscometer was designed, calibrated, and validated with an innovative combined laboratory-based and computational approach. The device proved to be a very useful tool with highly heterogeneous road paving materials, such as bituminous binders modified with crumb rubber powder, however authors strongly believe that DHR testing geometry can be adapted in many other applications. The following are the takeaway messages for those researchers facing similar issues and eager to develop and use a DHR in other sector of material science:

- The technical information and methods allowing each laboratory or technologist to independently design, manufacture and correctly use their own DHR:
- Design: the DHR has been shown to be the most suitable geometry to enhance mixing efficiency of highly heterogeneous fluids to be characterized by means of rotational viscometers. The optimal geometrical ratios for this mixing process have been identified as follows: c/D = 0.06, s/D = 0.9, w/D = 0.15 and validated by means of CFD simulations.
- Manufacturing: 3D Rapid prototyping allowed a cost-effective solution to optimize DHR final geometry, however precise manufacturing in stainless steel was necessary to test at temperature above 160°C (necessary for asphalt binders)
- The performed calibration was carried out by using the widest range of Newtonian and non-Newtonian fluids. This should allow technologist to use the calibration parameters, proposed in this investigation, also within their own field of study.

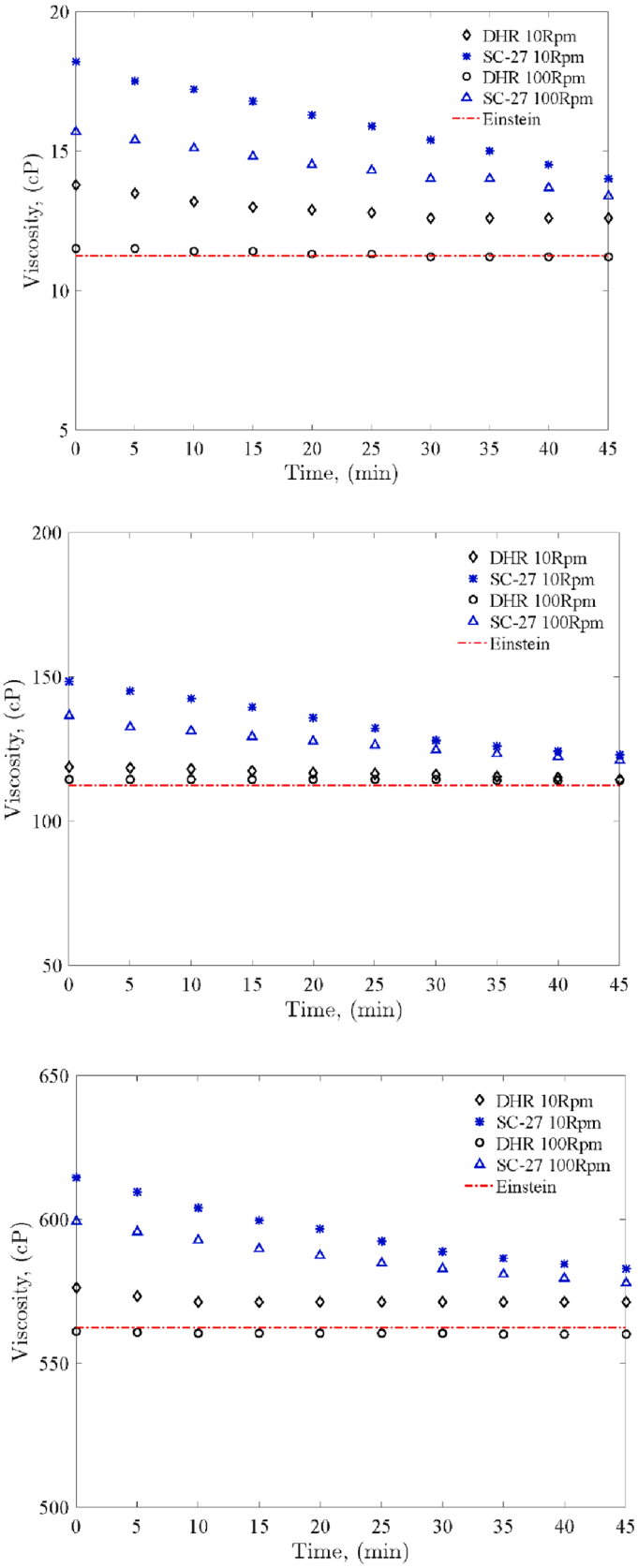

Fig. 5.2. Viscosity measurements by using Brookfield viscometer on standard fluid f10 (up) f100 (center) and f500 (bottom) plus 5% of suspended solids, the dotted red line indicates the viscosity values calculated by using the Einstein's equation (equation 30). (For interpretation of the references to colour in this figure legend, the reader is referred to the web version of this article.)

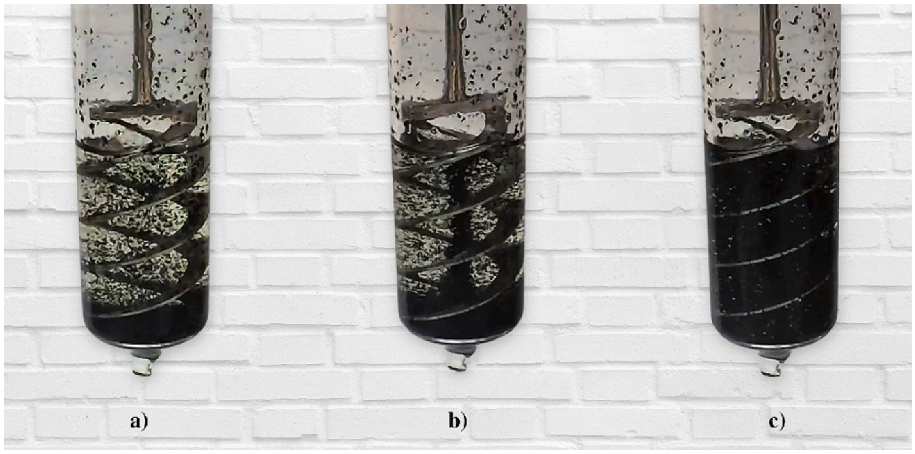

Fig. 5.3. DHR mixing process of a fluid with suspended particles at the start (a), after few seconds(b) and at the end (c).

- A validation procedure is mandatory whenever material scientists use a tailored design of the proposed DHR and/or will try to apply the proposed geometry with material other than asphalt binders.
- Implementing the use of DHR within the road paving material science allowed obtaining more realistic viscosity measurements of highly heterogeneous asphalt binders, as well as improving asphalt binder modification with crumb rubber in laboratory by means of real-time monitoring of material rheological properties.

It should be noted that this study focused specifically on the rotational viscometer setup. However, it is worth mentioning that the authors have also extended this concept to Dynamic Shear Rheometers (DSR). The findings and insights gained from this investigation can be applied to enhance the understanding and performance of DSR instruments as well. This demonstrates the potential for further advancements and applications of the developed concept beyond the rotational viscometer domain. The computational platform here introduced can also be further leveraged to reduce the need for laboratory equipment by developing a virtual rheometer capable of measuring materials rheological response. Authors are glad to share freely any necessary details with those material scientists willing to foster the discovery of novel applications for the characterization of highly heterogeneous fluids in any other sector.

CRediT authorship contribution statement

G. Giancontieri: Writing – review & editing, Writing – original draft, Methodology, Investigation, Data curation, Conceptualization. **D.M. Hargreaves:** Writing – review & editing, Validation, Supervision, Methodology, Formal analysis, Conceptualization. **P. Partal:** Writing – review & editing, Validation, Supervision, Methodology, Conceptualization. **D. Lo Presti:** Writing – review & editing, Supervision, Methodology, Data curation, Conceptualization.

Declaration of competing interest

The authors declare that they have no known competing financial interests or personal relationships that could have appeared to influence the work reported in this paper.

Data availability

Data will be made available on request.

References

[1] D. Lo Presti, C. Fecarotti, A. T. Clare, and G. Airey, "Toward more realistic viscosity measurements of tyre rubber–bitumen blends," *Constr. Build. Mater.*, vol. 67, Part B, no. 0, pp. 270–278, 2014.
[2] G. Giancontieri, D.M. Hargreaves, D. Lo Presti, Are we correctly measuring the rotational viscosity of heterogeneous bituminous binders? Road Mater. Pavement Des. (2019) S37–S56.
[3] T. G. Mezger, *The Rheology Handbook, 4th Edition*. 2014.
[4] A.Y. Malkin, The state of the art in the rheology of polymers: Achievements and challenges, Polym. Sci. Ser. A 51 (1) (2009) 80–102.
[5] R.B. Dow, The rheology of lubricants, J. Colloid Sci. (1946) 81–91.
[6] S. Bair, F. Qureshi, The high pressure rheology of polymer-oil solutions, Tribol. Int. 36 (2003) 637–645.
[7] S. Lin, R.S. Brodkey, Rheological Properties of Slurry Fuels, J. Rheol. N. Y. N. Y), vol. 29 (1985) 147.
[8] B. Celauro, C. Celauro, D. Lo Presti, A. Bevilacqua, Definition of a laboratory optimization protocol for road bitumen improved with recycled tire rubber, Constr. Build. Mater. 37 (2012) 562–572.
[9] J.G. Medina, G. Giancontieri, D. Lo Presti, Quality control of manufacturing and hot storage of crumb rubber modified binders, Constr. Build. Mater. 233 (2020) 1–12.
[10] M. Tušar, et al., RILEM TC 279 WMR round robin study on waste polyethylene modified bituminous binders: advantages and challenges, Road Mater. Pavement Des. (2022) 311–339.
[11] G. Giancontieri, S. Pouget, and D. Lo Presti, "Improved Testing Setup for Real-Time Monitoring of PMBs During Manufacturing and Rotational Viscosity Measurements," in *RILEM Bookseries*, 2022, vol. 27, pp. 1039–1045.
[12] D. Wang, et al., Rheological properties of asphalt binder modified with waste polyethylene: An interlaboratory research from the RILEM TC WMR, Resour. Conserv. Recycl. 186 (July) (2022) 1–16.
[13] D. Wang, et al., Rheological Behaviors of Waste Polyethylene Modified Asphalt Binder: Statistical Analysis of Interlaboratory Testing Results, J. Test. Eval. 51 (4) (2023) 1–12.
[14] D. Lo Presti, G. Airey, Tyre rubber-modified bitumens development : the effect of varying processing conditions, Road Mater. Pavement Des. 14 (4) (2013) 888–900.
[15] D. Lo Presti, G. Giancontieri, D.M. Hargreaves, Improving the rheometry of rubberized bitumen: experimental and computation fluid dynamics studies, Constr. Build. Mater. 136 (2017) 286–297.
[16] G. Giancontieri, D. M. Hargreaves, and D. Lo Presti, "Are we correctly measuring the rotational viscosity of rubberized bituminous binder ?," in *Proceedings of the Rubberised Asphalt - Asphalt Rubber 2018 Conference*, 2018.
[17] J. Gallego, G. Giancontieri, D. Lo Presti, Quality control of manufacturing and hot storage of crumb rubber modified binders, Constr. Build. Mater. 233 (2020) 1–12.
[18] C. Mignini, D. Lo Presti, G. Airey, A. Graziani, Rheological characterisation of cold bitumen emulsion slurries, Road Mater. Pavement Des., Jun. 22 (sup1) (2021) S232–S250.
[19] E. L. Paul, V. a Atiemo-obeng, and S. M. Kresta, *Handook of industrial mixing*. 2004.
[20] L. Choplin, P. Marchal, Mixwe-Type Rheometry, RHEOLOGY II (2007) 1–9.
[21] G.E. Cunningham, S. Deshpande, M.J.H. Simmons, J. O'Sullivan, Investigating mixer-viscometer techniques for partially filled stirred tanks, Chem. Eng. Sci. 282 (September) (2023) 1–11.
[22] G. Havas, J. Sawinsky, A. Deak, Investigation of homogenization efficency of the screw agitator, helical ribbon agitator, gate type anchor impeller and the multi-paddle agitator in the mixing of high-viscosity newtonian liquids, Period. Polytech. Chem. Eng. 22 (4) (1977) 317–330.
[23] G. Delaplace, J.C. Leuliet, V. Relandeau, Circulation and mixing times for helical ribbon impellers. Review and Experiments, Exp. Fluids 28 (2) (2000) 170–182.
[24] G. Delaplace, R. Guerin, J.C. Leuliet, R.P. Chhabra, An analytical model for the prediction of power consumption for shear-thinning fluids with helical ribbon and helical screw ribbon impellers, Chem. Eng. Sci. 61 (10) (2006) 3250–3259.

[25] Y. Tsui and Y. Hu, "Flow Characteristics in Mixers Agitated," vol. 429, no. 2011, pp. 416–429, 2011.
[26] M. Robinson, P.W. Cleary, Flow and mixing performance in helical ribbon mixers, Chem. Eng. Sci. 84 (2012) 382–398.
[27] Patterson, P. J. Carreau, and C. Y. Yap, "Mixing with helical ribbon agitators: Newtonian fluid," *AICHE J.*, vol. 25, no. 3, pp. 508–516, 1979.
[28] C.Y. Yap, W. Patterson, P.J. Carreau, Mixing with helical ribbon agitators: Non-Newtonian Fluids, AIChE J. 25 (3) (1979) 516–521.
[29] P. a Tanguy, R. Lacroix, F. Bertrand, L. Choplin, and E. B. D. La Fuente, "Finite element analysis of viscous mixing with a helical ribbon-screw impeller," *AICHE J.*, vol. 38, no. 6, pp. 939–944, 1992.
[30] K. Takahashi, K. Arai, S. Shozaburo, An extended power correlation for anchor and helical ribbon impellers, J. Chem. Eng. Japan (1982) 77–79.
[31] K. Takahashi, T. Yokota, H. Konno, Power Consumption of Helical Ribbon Agitators in Highly Viscous Pseudoplastic Liquids, J. Chem. Eng. Japan 17 (6) (1984) 657–659.
[32] F. Cordobes, E. Brito de la fuente, and C. Gallegos, "Effect of rheological properties on power input and effective shear rates when mixing with different impellers.," *An. química*, vol. 94, no. 4–5, pp. 274–278, 1998.
[33] K. Takahashi, T. Yokota, H. Konno, Mixing of pseudoplastic liquid in a vessel equipped with a variety of helical ribbon impellers, J. Chem. Eng. Japan 45 (1978) (1979) 63–68.
[34] K. Takahashi, M. Sasaki, K. Aria, S. Saito, Effects of Geometrical Variables of Helical Ribbon Impellers on Mixing of Highly Viscous Newtonian Liquids, J. Chem. Eng. Japan 15 (3) (1982) 217–224.
[35] P.J. Carreau, W.I. Patterson, C.Y. Yap, Mixing of viscoelastic fluids with helical-ribbon agitators I- Mixing time and flow patterns, Can. J. Chem. Eng. 54 (3) (1976) 135–142.
[36] M. Amiraftabi, M. Khiadani, H.A. Mohammed, Performance of a dual helical ribbon impeller in a two-phase (gas-liquid) stirred tank reactor, Chem. Eng. Process. - Process Intensif. 148 (September) (2019, 2020,) 1–13.
[37] Y. Tsui, Y. Hu, Flow Characteristics in Mixers Agitated, Eng. Appl. Comput. Fluid Mech. 5 (3) (2011) 416–429.
[38] J. De La Villéon, F. Bertrand, P. a. Tanguy, R. Labrie, J. Bousquet, and D. Lebouvier, "Numerical investigation of mixing efficiency of helical ribbons," *AIChE J.*, vol. 44, no. 4, pp. 972–977, 1998.
[39] H. Ameur, Y. Kamla, D. Sahel, Performance of helical ribbon and screw impellers for mixing viscous fluids in cylindrical reactors, ChemEngineering 2 (2) (2018) 1–9.
[40] B. Delacroix, L. Fradette, F. Bertrand, B. Blais, Which impeller should be chosen for efficient solid–liquid mixing in the laminar and transitional regime? AIChE J. 67 (11) (2021) 1–16.
[41] M. Amiraftabi, M. Khiadani, H. A. Mohammed, and A. Arshad, "CFD-PBM and experimental investigation of a shear thinning fluid in a gas-liquid tank agitated by a helical ribbon impeller," *Sep. Purif. Technol.*, vol. 272, no. December 2020, p. 118855, 2021.
[42] H. Furukawa, et al., Development and evaluation of mixing mechanism of new transformable multiple impeller (AM impeller), J. Adv. Manuf. Process. (July 2023) 1–13.
[43] A. Kazemzadeh, F. Ein-Mozaffari, A. Lohi, Mixing of highly concentrated slurries of large particles: Applications of electrical resistance tomography (ERT) and response surface methodology (RSM), Chem. Eng. Res. Des. 143 (2019) 226–240.
[44] A.L. Bowler, S. Bakalis, N.J. Watson, A review of in-line and on-line measurement techniques to monitor industrial mixing processes, Chem. Eng. Res. Des. 153 (2020) 463–495.
[45] M. Sommerfeld, S. Decker, State of the art and future trends in CFD simulation of stirred vessel hydrodynamics, Chem. Eng. Technol. 27 (3) (2004) 215–224.
[46] B. Um, T.R. Hanley, A CFD model for predicting the flow patterns of viscous fluids in a bioreactor under various operating conditions, Korean J. Chem. Eng 25 (5) (2008) 1094–1102.
[47] E. Brito-De La Fuente, L. Choplin, P. Tanguy, Mixing With Helical Ribbon Impellers, Chem. Eng. Res. Des. 75 (1) (1997) 45–52.
[48] V. Novak, F. Rieger, Homogenization with helical screw agitators, Trans. Inst. Chem. Eng. 47 (1969) 63–70.
[49] F. Rieger, V. Novak, Power consumption of agitators in highly viscous non-Newtonian liquids, Trans. Inst. Chem. Eng. 51 (1973) 105–111.
[50] M. Zhang, L. Zhang, B. Jiang, Y. Yin, X. Li, Calculation of Metzner Constant for Double Helical Ribbon Impeller by Computational Fluid Dynamic Method, Chinese J. Chem. Eng. 16 (5) (2008) 686–692.
[51] A.B. Metzner, R.E. Otto, Agitation of non-Newtonian fluids, AIChE J. 3 (1) (1957) 3–10.
[52] R.K. Thakur, C. Vial, G. Djelveh, M. Labbafi, Mixing of complex fluids with flat-bladed impellers: Effect of impeller geometry and highly shear-thinning behavior, Chem. Eng. Process. Process Intensif. 43 (10) (2004) 1211–1222.
[53] Ansys Inc., *Fluent User's Guide*. 2020.
[54] Y. Cengel and J. Cimbala, *Fluid mechanics: fundamentals and applications*. 2006.